Periodic smoothing splines for FFT-based solvers

Léo Morin [a,*], Renald Brenner [b], Katell Derrien [a], Khaoula Dorhmi [a]

[a] *Laboratoire PIMM, Arts et Metiers Institute of Technology, CNRS, Cnam, HESAM Universite, 151 boulevard de l'Hopital, 75013 Paris, France*

[b] *Sorbonne Université, CNRS, UMR 7190, Institut Jean Le Rond ∂′Alembert, F-75005 Paris, France*

Abstract

The aim of this paper is to develop a periodic smoother based on splines for FFT-based solvers. Spurious oscillations in FFT-based methods are shown to be due to pseudo-spectral differentiation of discontinuous fields. An automatic smoother based on polynomial splines is developed, which permits to add smoothness to initial material properties. The method, which is applied in various problems including conductivity, elasticity and field dislocation mechanics, improves significantly the local fields and reduces spurious oscillations.

Keywords: Fourier transforms; Smoothing splines; Spurious oscillations; Local fields

1 Introduction

Fast Fourier transform (FFT) – based methods constitute an efficient alternative to the finite element method (FEM) for solving physical problems governed by elliptic equations. This class of methods has been initially developed in the seminal paper of Moulinec and Suquet (1998) to determine the local and overall mechanical responses of linear and nonlinear composites with a periodic microstructure. The major advantages of the method are that (i) calculations can be easily performed, without any processing, from imagery techniques such as scanning electron microscopy (SEM) and tomography and do not require any meshing operations in contrast to FEM and (ii) the algorithm itself is much more efficient than the finite element method since it relies on the computational complexity of fast Fourier transforms that is lower than matrix-assembled methods. Accelerated iterative schemes (Eyre and Milton, 1999; Michel et al., 2000; Monchiet and Bonnet, 2012; Moulinec and Silva, 2014) have been developed in order to overcome the low convergence rate of the basic scheme for highly constrasted materials, allowing this method to be a viable and attractive alternative to the finite-element method in the context of microstructure simulations; the method has been notably successfully applied in numerous types of problems: elasticity (Moulinec and Suquet, 1998), J2-plasticity (Moulinec and Suquet, 1998), crystal (elasto)viscoplasticity (Lebensohn, 2001; Suquet et al., 2012), dislocation-mediated plasticity (Brenner et al., 2014; Berbenni et al., 2014; Bertin et al., 2015), conductivity (Eyre and Milton, 1999), ferroelectricity (Brenner, 2009; Vidyasagar et al., 2017), among others.

* Corresponding author.
Email address: leo.morin@ensam.eu (Léo Morin).

Despite its important success, the method suffers from some drawbacks. An important issue is the presence of spurious oscillations on some local fields, in the presence of material discontinuities. This was observed in various cases, including conductivity (Willot et al., 2014), elasticity (Gélébart and Ouaki, 2015; Willot, 2015) and field dislocation mechanics (Brenner et al., 2014; Berbenni et al., 2014). Attributed to a "Gibbs" phenomenon or aliasing, these oscillations are problematic when local fields are seeked and may lead to important discrepancies in specific problems. For instance, in dislocation-mediated plasticity, the local stress field calculated by FFT serves in an hyperbolic Hamilton-Jacobi system of equations to transport dislocation densities (Morin et al., 2019), which are known to be very sensitive to oscillations. Different remedies have been proposed to reduce oscillations:

(1) *Modified Green operators* have been introduced to replace the classical continuous Green operator used in the basic scheme of Moulinec and Suquet (1998). Discrete Green operators are constructed from a finite difference discretization of partial derivatives instead of pseudo-spectral differentiation. Several versions have been studied, with centered finite differences (Müller, 1996; Brown et al., 2002; Berbenni et al., 2014; Eloh et al., 2018), forward and backward differences (Willot et al., 2014; Willot, 2015), among others. In most cases, an improvement of both the local fields and the iterative procedure is observed.
(2) *An Interphase approach* has been proposed to improve spatial converge and reduce non-physical oscillations (Gélébart and Ouaki, 2015; Kabel et al., 2015; Charière et al., 2020; Wang et al., 2020). It consists in the introduction of homogenized properties on pixels located at the crossing of material interfaces. This method requires the prior detection of interfaces and the definition of a unique normal vector in each composite voxel.

An alternative approach is considered in this work. It consists in the data filtering of the discontinuous fields responsible for oscillations. Data filtering encompasses a large body of methods, including (non-exhaustively) non-linear filters to remove oscillations (Vandeven, 1991; Cai et al., 1992), Laplace operators to detect edge in noisy signals (van Vliet et al., 1989), and data smoothing. In this work, we will focus on data smoothing techniques because it allows to circumvent the problem of oscillations following two different paths, (i) by reducing material discontinuities or (ii) by removing oscillations (acting as noise) on the solution fields. Indeed data smoothing has been initially developed to separate *smooth* patterns in data from the *rough* sequence corresponding to (experimental) noise. A great number of techniques has been developed to perform data smoothing, based on kernel regression (Hastie and Loader, 1993), polynomial regression (Savitzky and Golay, 1964), attenuation factors (Berrut and Reifenberg, 1997) and polynomial smoothing splines (Schoenberg, 1964; Craven and Wahba, 1979; Buckley, 1994), among others. In the context of FFT-based solvers applied to field dislocation mechanics, it is worth noting that Brenner et al. (2014) proposed to spread the dislocation density corresponding to pixel-wise single dislocations on a surface of 3×3 pixels. This spreading, which has resulted in a significant decrease of oscillations, can be seen as a manual smoothing of the initial dislocation density field. The aim of this paper is to provide a robust and automatic periodic smoother, that can be applied to an arbitrary microstructure, in order to reduce artifacts in the description of local fields. In this regard, polynomial smoothing splines are very attractive because they are constructed from the minimization of a functional that balances the fidelity to the data and the smoothness of the estimate. The smoothness can thus be easily controlled by a single scalar parameter. The advantage of such data smoothing is that it permits to operate once and for all on initial microstructures or on the solution fields, and does not require any modification of the FFT-based solver.

The paper is organized as follows. In Section 2, several physical problems of interest as well as the basics of FFT-based solvers are presented. The problem of spurious oscillations is analyzed in Section 3. A periodic spline smoother is then developed in Section 4. Finally, the smoother is applied to problems of conductivity, elasticity and field dislocation mechanics in Section 5.

2 Preliminaries

2.1 Physical problems of interest

We are concerned in solving the equations of different physical problems (conductivity, elasticity and field dislocation mechanics theory) in infinite periodic media. The unit-cell is a square or cubic domain $\Omega = [-L/2,\ L/2]^d$ ($d = 2$ or 3) with L the period of the microstructure. Tensorial components refer to a system of Cartesian coordinates $(\mathbf{e}_1;\mathbf{e}_2)$ in 2D and $(\mathbf{e}_1;\mathbf{e}_2;\mathbf{e}_3)$ in 3D.

2.1.1 Conductivity

The problem of conductivity, which can be considered as a model problem for studying FFT-based solvers (Willot et al., 2014), consists in the computation of the electric field $\mathbf{E}(\Phi(\boldsymbol{x}))$, current $\mathbf{J}(\boldsymbol{x})$ and electric potential $\Phi(\boldsymbol{x})$, at each point $\boldsymbol{x}$ in Ω, for a given conductivity field $\boldsymbol{c}(\boldsymbol{x})$. A unit-cell with periodic boundary conditions is considered and the local electric field $\mathbf{E}$ is split into its average $\overline{\mathbf{E}} = \langle\mathbf{E}\rangle$ (where $\langle\cdot\rangle$ denotes the spatial average over Ω) and a fluctuation term $\mathbf{E}(\Phi^*(\boldsymbol{x}))$:

$$\mathbf{E}(\Phi(\boldsymbol{x})) = \mathbf{E}(\Phi^*(\boldsymbol{x})) + \overline{\mathbf{E}} \qquad \text{or equivalently} \qquad \Phi(\boldsymbol{x}) = \Phi^*(\boldsymbol{x}) - \overline{\mathbf{E}}.\boldsymbol{x}. \tag{1}$$

Periodic boundary conditions assume that the fluctuating part Φ^* is periodic (notation: $\Phi^*\#$) and that the term $\mathbf{J}.\boldsymbol{n}$ is anti-periodic on the boundary between two neighboring cells with $\boldsymbol{n}$ the outer normal along the boundary $\partial\Omega$ of Ω (notation: $\mathbf{J}.\boldsymbol{n} - \#$). The local problem to be solved is

$$\begin{cases} \operatorname{div}\mathbf{J}(\boldsymbol{x}) &= 0 \\ \mathbf{J}(\boldsymbol{x}) &= \boldsymbol{c}(\boldsymbol{x}) : \left(\mathbf{E}(\Phi^*(\boldsymbol{x})) + \overline{\mathbf{E}}\right) \\ \mathbf{E}\left(\Phi^*(\boldsymbol{x})\right) &= -\boldsymbol{\nabla}\Phi^*(\boldsymbol{x}), \end{cases} \tag{2}$$

where $\boldsymbol{c}(\boldsymbol{x})$ is the local second-order conductivity tensor. In the particular case of isotropic conductivity, it reads

$$\boldsymbol{c}(\boldsymbol{x}) = c(\boldsymbol{x})\mathbf{I}_3 \tag{3}$$

with $c(\boldsymbol{x})$ the local (scalar) conductivity field and $\mathbf{I}_3$ the second-order identity tensor.

2.1.2 Elasticity

The problem of elasticity consists in the computation of the elastic strain $\varepsilon(\boldsymbol{u}(\boldsymbol{x}))$, stress $\boldsymbol{\sigma}(\boldsymbol{x})$ and displacement field $\boldsymbol{u}(\boldsymbol{x})$, at each point $\boldsymbol{x}$ in Ω, for a given elasticity field $\mathbb{C}(\boldsymbol{x})$. The local strain $\varepsilon(\boldsymbol{x})$ is split into its average $\overline{\varepsilon}$ and a fluctuation term $\varepsilon(\boldsymbol{u}^*(\boldsymbol{x}))$:

$$\varepsilon(\boldsymbol{u}(\boldsymbol{x})) = \varepsilon(\boldsymbol{u}^*(\boldsymbol{x})) + \overline{\varepsilon} \qquad \text{or equivalently} \quad \boldsymbol{u}(\boldsymbol{x}) = \boldsymbol{u}^*(\boldsymbol{x}) + \overline{\varepsilon}.\boldsymbol{x}. \tag{4}$$

The fluctuating part $\boldsymbol{u}^*(\boldsymbol{x})$ is periodic (notation: $\boldsymbol{u}^*(\boldsymbol{x})\#$) and the stress vector $\boldsymbol{\sigma}.\boldsymbol{n}$ is anti-periodic on the boundary between two neighboring cells with $\boldsymbol{n}$ the outer normal along the boundary $\partial\Omega$ of Ω (notation: $\boldsymbol{\sigma}.\boldsymbol{n} - \#$). The local problem to be solved is

$$\begin{cases} \text{div}\, \boldsymbol{\sigma}(\boldsymbol{x}) &= 0 \\ \boldsymbol{\sigma}(\boldsymbol{x}) &= \mathbb{C}(\boldsymbol{x}) : (\boldsymbol{\varepsilon}(\boldsymbol{u}^*(\boldsymbol{x})) + \overline{\boldsymbol{\varepsilon}}) \\ \boldsymbol{\varepsilon}(\boldsymbol{u}^*(\boldsymbol{x})) &= \dfrac{1}{2}\left(\boldsymbol{\nabla}\boldsymbol{u}^* + \boldsymbol{\nabla}^T\boldsymbol{u}^*\right), \end{cases} \tag{5}$$

where $\mathbb{C}(\boldsymbol{x})$ is the fourth-order stiffness tensor. In the particular case of isotropic elasticity, it reads

$$\mathbb{C}(\boldsymbol{x}) = 3\kappa(\boldsymbol{x})\mathbb{J} + 2\mu(\boldsymbol{x})\mathbb{K}, \tag{6}$$

with $\kappa(\boldsymbol{x})$ and $\mu(\boldsymbol{x})$ are respectively the local bulk and shear moduli. $\mathbb{J}$ and $\mathbb{K}$ are linearly independent isotropic tensors defined by

$$\mathbb{J} = \frac{1}{3}\mathbf{I}_3 \otimes \mathbf{I}_3, \quad \mathbb{K} = \mathbb{I} - \mathbb{J}, \tag{7}$$

with $\mathbb{I}$ the fourth order identity tensor.

2.1.3 Field Dislocations Mechanics

We finally consider the problem of field dislocation mechanics (FDM) (Acharya, 2001; Brenner et al., 2014; Djaka et al., 2020), which consists in finding, for given periodic dislocation density field $\boldsymbol{\alpha}(\boldsymbol{x})$ and elasticity field $\mathbb{C}(\boldsymbol{x})$, the internal stress $\boldsymbol{\sigma}(\boldsymbol{x})$, elastic strain $\boldsymbol{\varepsilon}(\boldsymbol{u}(\boldsymbol{x}))$ and displacement fields $\boldsymbol{u}(\boldsymbol{x})$, $\forall \boldsymbol{x} \in \Omega$. The problem to be solved reads

$$\begin{cases} \textbf{div}\, \boldsymbol{\sigma}(\boldsymbol{x}) &= \mathbf{0} \\ \boldsymbol{\sigma}(\boldsymbol{x}) &= \mathbb{C}(\boldsymbol{x}) : (\boldsymbol{\varepsilon}(\boldsymbol{u}^*(\boldsymbol{x})) + \overline{\boldsymbol{\varepsilon}}) + \boldsymbol{\tau}(\boldsymbol{x}) \\ \boldsymbol{\varepsilon}(\boldsymbol{u}^*(\boldsymbol{x})) &= \dfrac{1}{2}\left(\boldsymbol{\nabla}\boldsymbol{u}^* + \boldsymbol{\nabla}^T\boldsymbol{u}^*\right) \end{cases} \tag{8}$$

where the (prescribed) periodic polarization tensor $\boldsymbol{\tau}(\boldsymbol{x})$ is defined by

$$\boldsymbol{\tau}(\boldsymbol{x}) = \mathbb{C}(\boldsymbol{x}) : \boldsymbol{\chi}(\boldsymbol{x}) \quad \text{with} \quad \textbf{curl}\, \boldsymbol{\chi}(\boldsymbol{x}) = \boldsymbol{\alpha}(\boldsymbol{x}). \tag{9}$$

$\boldsymbol{\chi}(\boldsymbol{x})$ is the incompatible part of the elastic distortion of the crystalline lattice related to the presence of dislocations. It is responsible of the internal stress state within the material in the absence of applied mechanical loading. It can be noted that the local constitutive law in (8) is similar to "thermoelasticity" (i.e local elastic behaviour with a prescribed eigenstress field).

2.2 Principles of FFT-based schemes

The basic scheme of Moulinec and Suquet (1998) is briefly presented in the case of isotropic conductivity under prescribed macroscopic electric field $\overline{\mathbf{E}}$, for simplicity purpose.

The periodic Lippman-Schwinger equation First, the problem of conductivity is alternatively written as the auxiliary problem

$$\begin{cases} \operatorname{div} \mathbf{J}(\boldsymbol{x}) &= 0 \\ \mathbf{J}(\mathbf{x}) &= c^0 \left(\mathbf{E}(\Phi^*(\boldsymbol{x})) + \overline{\mathbf{E}} \right) + \boldsymbol{\tau}(\boldsymbol{x}) \\ \mathbf{E}\left(\Phi^*(\mathbf{x})\right) &= -\boldsymbol{\nabla}\Phi^*(\mathbf{x}), \end{cases} \tag{10}$$

where the polarization tensor $\boldsymbol{\tau}(\boldsymbol{x}) = (c(\boldsymbol{x}) - c^0) \left(\mathbf{E}(\Phi^*(\boldsymbol{x})) + \overline{\mathbf{E}} \right)$ and c_0 is the conductivity of some homogeneous reference medium.

The auxiliary problem reduces to the periodic Lippmann-Schwinger equation and can be easily solved provided that the polarization tensor $\boldsymbol{\tau}(\boldsymbol{x})$ is known. The electric field can be derived in real space by means of the periodic Green operator $\boldsymbol{\Gamma}^0$ associated with c^0

$$\mathbf{E}(\Phi^*(\boldsymbol{x})) = -\boldsymbol{\Gamma}^0(\boldsymbol{x}) * \boldsymbol{\tau}(\boldsymbol{x}), \tag{11}$$

or equivalently in Fourier space

$$\widehat{\mathbf{E}}(\boldsymbol{\xi}) = -\widehat{\boldsymbol{\Gamma}}^0(\boldsymbol{\xi}) : \widehat{\boldsymbol{\tau}}(\boldsymbol{\xi}) \quad \forall \xi \neq \mathbf{0}, \quad \widehat{\mathbf{E}}(\mathbf{0}) = \overline{\mathbf{E}}, \tag{12}$$

where $\boldsymbol{\xi}$ denotes the frequency in Fourier space associated to the point $\boldsymbol{x}$. It is worth noting that the Green operator has an explicit form in Fourier space:

$$\widehat{\boldsymbol{\Gamma}}^0(\boldsymbol{\xi}) = \frac{\boldsymbol{\xi} \otimes \boldsymbol{\xi}}{c^0 |\boldsymbol{\xi}|^2}. \tag{13}$$

The last step is to determine the polarization tensor $\boldsymbol{\tau}(\boldsymbol{x})$ solution of the problem, which verifies $\boldsymbol{\tau}(\boldsymbol{x}) = (c(\boldsymbol{x}) - c^0) \left(\mathbf{E}(\Phi^*(\boldsymbol{x})) + \overline{\mathbf{E}} \right)$. This can be performed by means of an iterative scheme.

The iterative scheme The basic scheme of Moulinec and Suquet (1998) consists in a fixed point in order to determine $\boldsymbol{\tau}(\boldsymbol{x})$. The following algorithm is thus considered:

$$\begin{cases} \text{Initialization} & \mathbf{E}^0(\boldsymbol{x}) = \overline{\mathbf{E}} \\ & \mathbf{J}^0(\boldsymbol{x}) = c(\boldsymbol{x}) \mathbf{E}^0(\boldsymbol{x}) \\ \text{Iterate i + 1} & \mathbf{E}^i \text{ and } \mathbf{J}^i \text{ being known} \\ \text{(a)} & \boldsymbol{\tau}^i(\boldsymbol{x}) = \mathbf{J}^i(\boldsymbol{x}) - c^0 \mathbf{E}^i(\boldsymbol{x}) \\ \text{(b)} & \widehat{\boldsymbol{\tau}}^i = \mathcal{F}\left(\boldsymbol{\tau}^i\right) \\ \text{(c)} & \text{Convergence test} \\ \text{(d)} & \widehat{\mathbf{E}}^{i+1}(\boldsymbol{\xi}) = -\widehat{\boldsymbol{\Gamma}}^0(\boldsymbol{\xi}) : \boldsymbol{\tau}^i(\boldsymbol{\xi}) \; \forall \xi \neq \mathbf{0} \quad \text{and } \widehat{\mathbf{E}}^{i+1}(\mathbf{0}) = \overline{\mathbf{E}} \\ \text{(e)} & \mathbf{E}^{i+1} = \mathcal{F}^{-1}\left(\widehat{\mathbf{E}}^{i+1}\right) \\ \text{(f)} & \mathbf{J}^{i+1}(\boldsymbol{x}) = c(\boldsymbol{x}) \mathbf{E}^{i+1} \end{cases} \tag{14}$$

Convergence is reached when $\mathbf{J}^{i+1}$ is in equilibrium. In practice, the iterative procedure is stopped when the error serving to check convergence (Moulinec and Suquet, 1998)

$$e^i = \frac{\left(\left\langle \left\| \mathrm{div}(\mathbf{J}^i) \right\|^2 \right\rangle\right)^{1/2}}{||\langle \mathbf{J}^i \rangle||} \tag{15}$$

is smaller than a prescribed (small) value (typically 10^{-5} in practice).

3 Spurious oscillations in local fields

3.1 The problem of pseudo-spectral differentiation

Generalities Let us consider the problem of two-dimensional conductivity with homogeneous conductivity c^0 subjected to an heterogeneous polarization tensor field $\boldsymbol{\tau}(\boldsymbol{x})$. It will shed light on how spurious oscillations may emerge on local fields computed by FFT-based methods[1]. The problem to be solved, which consists in finding the fluctuation of the electric field $\mathbf{E}(\Phi(\boldsymbol{x}))$, current $\mathbf{J}(\boldsymbol{x})$ and electric potential $\Phi^*(\boldsymbol{x})$ in a periodic Ω, thus reduces to

$$\begin{cases} \mathrm{div}\, \mathbf{J}(x_1, x_2) = 0 \\ \mathbf{J}(x_1, x_2) \quad = c^0 \mathbf{E}^*(x_1, x_2) + \boldsymbol{\tau}(x_1, x_2) \\ \mathbf{E}^*(x_1, x_2) \quad = -\boldsymbol{\nabla} \Phi^*(x_1, x_2). \end{cases} \tag{16}$$

The electric potential Φ^* that solves this system is the solution of the following Poisson equation

$$\Delta \Phi^* = \frac{1}{c^0} \left(\frac{\partial \tau_1}{\partial x_1} + \frac{\partial \tau_2}{\partial x_2} \right). \tag{17}$$

Let us assume now that the polarization tensor $\boldsymbol{\tau}$ has discontinuities. In that case it is easy to show that the solution Φ^* may not have necessarily continuous derivatives. For instance in the particular case

$$\tau_1(x_1, x_2) = -2\frac{1}{x_1^3 x_2^2} - 6\frac{1}{x_1 x_2^4}, \quad \tau_2(x_1, x_2) = 0, \quad c_0 = 1, \tag{18}$$

the solution of the Poisson equation Φ^* is of the form

$$\Phi^*(x_1, x_2) = \frac{1}{x_1^2 x_2^2} + K_1 x_1 + K_2 x_2 + K_3, \tag{19}$$

where K_1, K_2 and K_3 are constants. Thus, in that case Φ^* is not C^1 (where C^1 consists of all differentiable functions whose derivative is continuous). This may have critical consequences upon the determination of the partial derivatives $\partial \Phi^* / \partial x_1$ and $\partial \Phi^* / \partial x_2$ since in practice they are computed in Fourier space using pseudo-spectral differentiation. Since Φ^* is not necessarily

[1] In the case where $\boldsymbol{\tau} = \left(c(x_1, x_2) - c^0\right) \overline{\mathbf{E}}$, this problem corresponds to the initial step of the basic scheme of the heterogeneous problem of conductivity (with heterogeneous $c(x_1, x_2)$).

C^1, the computation of the derivatives $\partial\Phi^*/\partial x_1$ and $\partial\Phi^*/\partial x_2$ may thus generate numerical spurious oscillations. Indeed, since pseudo-spectral differentiation corresponds to the limit of finite difference of increasing order (Fornberg, 1987), it produces strong oscillations at the crossing of a derivative jump, which only dies down as $O(x)$ where x is the distance to the jump. Thus the presence of discontinuities can lead to derivative jumps which may be the origins of spurious oscillations.

An example To illustrate this, we consider the resolution of equation (17) in a more simple numerical example to highlight the occurrence of oscillations even with "low" discontinuities. We consider a periodic 2D domain $[-1,\ 1] \times [-1,\ 1]$, discretized with 64×64 pixels, in which the distribution of the polarization tensor is uniform in the whole domain except in a small square domain of size 5×5 pixels (see Figure 1):

$$\tau_1 = \begin{cases} 10 \text{ if } |x_1| \leq 0.0625 \text{ or } |x_2| \leq 0.0625 \\ 1 \quad \text{elsewhere} \end{cases}, \quad \tau_2 = 0. \tag{20}$$

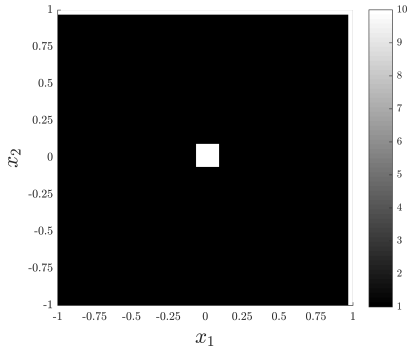

Fig. 1. Distribution of the component τ_1 of the polarization tensor.

We consider the resolution of equation (17) using pseudo-spectral differentiation. The electrical field Φ^* and the partial derivatives $\partial\Phi^*/\partial x_1$ and $\partial\Phi^*/\partial x_2$, which are deduced using pseudo-spectral differentiation, are represented in Figure 2.

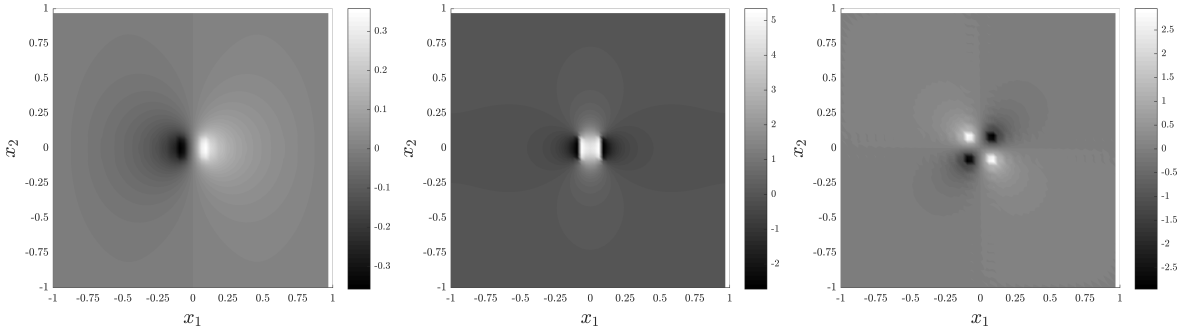

(a) (b) (c)

Fig. 2. Distributions of the (a) Electrical field Φ^* computed using pseudo-spectral differentiation, (b) Partial derivative $\partial\Phi^*/\partial x_1$ computed using pseudo-spectral differentiation and (c) Partial derivative $\partial\Phi^*/\partial x_2$ computed using pseudo-spectral differentiation.

Spurious oscillations can be exhibited with an enlarged view of the partial derivative $\partial\Phi^*/\partial x_2$ on the lines $x_2 \approx 0.0625$ (at the inclusion's boundary) and $x_2 \approx 1$ represented in Figure 3.

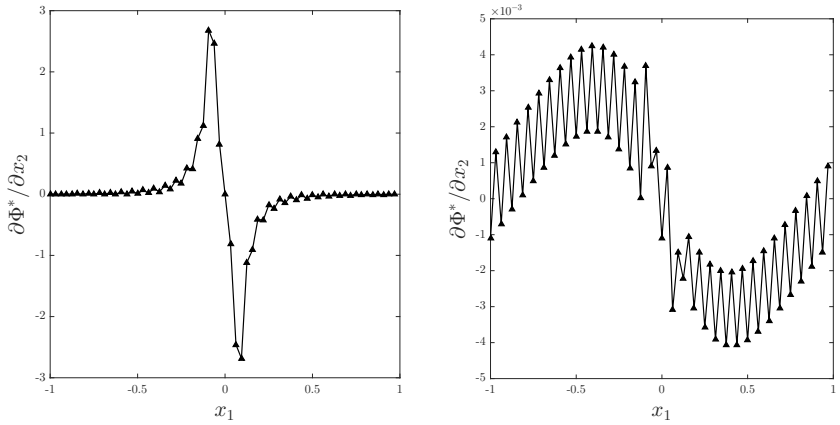

(a) (b)

Fig. 3. Partial derivative $\partial\Phi^*/\partial x_2$ computed using pseudo-spectral differentiation on the lines (a) $x_2 \approx 0.0625$ and (b) $x_2 \approx 1$.

3.2 Discussion

It has been shown that spurious oscillations may initiate in FFT-based solvers when the polarization field exhibits discontinuities, and thus it may emerge at each step of the iterative procedure. Thus, oscillations may appear when material properties have discontinuities (since the polarization tensor depends on local properties field) and when pseudo-spectral differentiation is used for the resolution of the elliptic equation. It thus appears that two ways may improve the computation of local fields:

(1) the smoothing of material properties should permit to erase discontinuities and thus should not induce any oscillations while solving the elliptic equation;
(2) the use of suitable differentiation operators that are not sensitive to strong discontinuities, should also erase oscillations due to differentiation.

The latter has been explored in previous studies. Discrete Green operators, which are constructed from finite differences, appear suitable to improve local fields since they may overcome the difficulties of pseudo-spectral differentiation in presence of strong discontinuities. Several discrete Green operators (Brisard and Dormieux, 2012; Willot et al., 2014; Berbenni et al., 2014; Willot, 2015) have been shown to successfully erase the occurrence of oscillations. However, at the crossing of the material jump, nothing prevent finite differences to induce small oscillations or discrepancies as it was shown in elasticity problems (Schneider, 2020).

In the present work, we investigate the alternative way which consists in reducing material discontinuities responsible for derivative jumps. This is particularly attractive for the following reasons:

- it permits to keep pseudo-spectral rules for differentiation and thus enable a better accuracy than finite-differences;
- it is physically meaningful since in practice there is an interphase between two phases;
- it does not require any modifications of the FFT-based solvers but only a smooth microstructure as an input of the calculation.

This initial smoothing of the discontinuous material fields will be termed *pre-smoothing* of the microstructure.

It is worth noting that smoothing techniques can also be applied on the solution field having oscillations, where the oscillations can be seen as "noise". In that case, the smoothing is a post-treatment made on the solution field exhibiting oscillations and will be termed *post-smoothing*.

4 Smoothing of evenly spaced periodic data

The aim of this Section is to develop a robust and systematic method for smoothing evenly spaced periodic data in a one-dimensional case. In this Section, the system of Cartesian coordinates is denoted by $(\mathbf{e}_x, \mathbf{e}_y)$ in 2D and $(\mathbf{e}_x, \mathbf{e}_y, \mathbf{e}_z)$ in 3D, for simplicity.

4.1 One-dimensional case

We are concerned with the smoothing of a periodic unidimensional function f with period T, defined in the interval $[0,\ T]$ discretized with N segments. We consider a uniform grid with spatial scale $\Delta x = T/N$ and we use the following notations: $x_j = j\Delta x$, $f_j = f(x_j)$, with $0 \leq j \leq N-1$. The discrete values of function f denoted f_j may thus be written as a vector $\boldsymbol{f}$ of size N. The smooth estimate is denoted by $\tilde{f}$, and we are thus looking for its discrete values $\tilde{f}_i$ which consists in finding the vector $\tilde{\boldsymbol{f}} = [\tilde{f}_0, \tilde{f}_1, ..., \tilde{f}_{N-1}]$.

4.1.1 Preliminaries

We recall some basic but important relations related to Fourier analysis. The discrete Fourier transform of $\boldsymbol{f}$, denoted by $\mathrm{DFT}(\boldsymbol{f})$, is the vector $\widehat{\boldsymbol{f}}$ defined by

$$\widehat{\boldsymbol{f}} = \mathrm{DFT}(\boldsymbol{f}) = \mathbf{F}\boldsymbol{f}, \tag{21}$$

where $\mathbf{F}$ is the classical $N \times N$ "DFT matrix" whose components are given by

$$F_{jk} = \exp\left(\frac{2\pi\imath}{N} jk\right), \tag{22}$$

where $\imath$ is the imaginary unit. The inverse discrete Fourier transform, denoted by IDFT, is defined such as

$$\boldsymbol{f} = \mathrm{IDFT}(\widehat{\boldsymbol{f}}) = \mathbf{F}^{-1}\widehat{\boldsymbol{f}}, \tag{23}$$

where $\mathbf{F}^{-1}$ is the inverse matrix of $\mathbf{F}$ verifying

$$\mathbf{F}\mathbf{F}^{-1} = \mathbf{F}^{-1}\mathbf{F} = \mathbf{I}_N, \tag{24}$$

where $\mathbf{I}_N$ is the $N \times N$ identity matrix. It is interesting to note that $\mathbf{F}^{-1}$ can be expressed in terms of the conjugate matrix of $\mathbf{F}$ (denoted by $\overline{\mathbf{F}}$) such as:

$$\mathbf{F}^{-1} = \frac{1}{N}\overline{\mathbf{F}}. \tag{25}$$

The vector containing the values of the derivative $f'(x_j)$ of f at the grid points, denoted by $\boldsymbol{f}'$, can be determined in Fourier space using pseudo-spectral differentiation:

$$\widehat{\boldsymbol{f}}' = \imath\boldsymbol{\xi} \circ \widehat{\boldsymbol{f}}, \tag{26}$$

where $\boldsymbol{\xi}$ is the vector containing the discrete frequencies associated with $\boldsymbol{x}$ and $\circ$ denotes Hadamard product (pointwise product). Equation (26) equivalently writes

$$\widehat{\boldsymbol{f}'} = \imath \boldsymbol{\Lambda} \widehat{\boldsymbol{f}}, \tag{27}$$

where $\boldsymbol{\Lambda}$ is the diagonal matrix containing the discrete Fourier frequencies:

$$\Lambda_{ii} = \xi_i, \quad \Lambda_{ij} = 0 \text{ if } i \neq j. \tag{28}$$

In the real space, the derivative $\boldsymbol{f}'$ can be written such as

$$\boldsymbol{f}' = \imath \mathbf{F}^{-1} \boldsymbol{\Lambda} \mathbf{F} \boldsymbol{f}, \tag{29}$$

which permits the definition of the pseudo-spectral differentiation operator.

4.1.2 Spline smoothing of evenly spaced gridded data

For the objective of this work, which is to smooth out the fields involved in FFT-based methods, polynomial smoothing splines appear very attractive since they permit to construct a smooth estimate $\tilde{f}$ of f with continuous derivatives up to some order.

Smoothing splines are the solution of the minimization of a functional that balances the fidelity to the data, through the residual sum-of-squares (RSS), and the smoothness of the estimate, through some penalty term (Craven and Wahba, 1979)

$$\frac{1}{N} \sum_{j=0}^{N-1} \left(f(x_j) - \tilde{f}(x_j) \right)^2 + \frac{s}{T} \int_0^T \left(\tilde{f}^{(m)}(u) \right)^2 \mathrm{d}u. \tag{30}$$

The solution of the minimization problem (30) is a polynomial smoothing spline of degree $2m - 1$ (Schoenberg, 1964; Craven and Wahba, 1979). The parameter s controls the tradeoff between the "smoothness" of the solution and the fidelity to the data.

The integral in equation (30) can be approximated by a trapezoidal rule which leads to the functional

$$\mathcal{F}\left(\tilde{\boldsymbol{f}}\right) = \left\| \boldsymbol{f} - \tilde{\boldsymbol{f}} \right\|^2 + s \left\| \tilde{\boldsymbol{f}}^{(m)} \right\|^2, \tag{31}$$

where $\|\|$ denotes the Euclidean norm. The functional defined by (31) is generally referred as the "discontinuous setting" where the penalty term is expressed as the sum of squares of the point-values of the $m-$th derivative (Whittaker, 1922; Eilers, 2003; Garcia, 2010). With some appropriate differentiation rule, the discontinuous setting is very interesting because it permits to express the penalty term as a linear combination of the $\tilde{f}_j = \tilde{f}(x_j)$, which allows to solve the minimization problem quite easily. In previous works, two-points finite differences were considered (Buckley, 1994; Eilers, 2003; Garcia, 2010). In the context of FFT-based solvers, the differentiation rule considered is naturally the pseudo-spectral differentiation (which corresponds to a finite-difference method of increasing accuracy (Fornberg, 1987)). The penalty term thus reads

$$\left\| \tilde{\boldsymbol{f}}^{(m)} \right\|^2 = \left\| \mathbf{D} \tilde{\boldsymbol{f}} \right\|^2, \tag{32}$$

where the differentiation matrix $\mathbf{D}$ is obtained from equation (29) and reads

$$\mathbf{D} = \imath^m \mathbf{F}^{-1} \boldsymbol{\Lambda}^m \mathbf{F}. \tag{33}$$

Using equations (31) and (32), the minimization of $\mathcal{F}$ leads to the following linear system

$$\left(\mathbf{I}_N + s\overline{\mathbf{D}}^{\mathrm{T}}\mathbf{D}\right)\tilde{\boldsymbol{f}} = \boldsymbol{f}, \tag{34}$$

where $\overline{\mathbf{D}}^{\mathrm{T}}$ is the conjugate transpose of $\mathbf{D}$. Using equations (25) and (33), it is readily seen that $\overline{\mathbf{D}}^{\mathrm{T}}$ is of the form

$$\overline{\mathbf{D}}^{\mathrm{T}} = -i^m \mathbf{F}^{-1}\boldsymbol{\Lambda}^m\mathbf{F}. \tag{35}$$

Equation (34) can thus be rewritten

$$\mathbf{F}^{-1}\left(\mathbf{I}_N + s\boldsymbol{\Lambda}^{2m}\right)\mathbf{F}\tilde{\boldsymbol{f}} = \boldsymbol{f}, \tag{36}$$

which implies that the smooth estimate $\tilde{\boldsymbol{f}}$ reads

$$\tilde{\boldsymbol{f}} = \mathbf{F}^{-1}\left(\mathbf{I}_N + s\boldsymbol{\Lambda}^{2m}\right)^{-1}\mathbf{F}\boldsymbol{f}. \tag{37}$$

By taking advantage of the definition of the discrete Fourier transform and inverse discrete Fourier transform, respectively given by equations (21) and (23), the smooth estimate $\tilde{\boldsymbol{f}}$ finally reads

$$\tilde{\boldsymbol{f}} = \mathrm{IDFT}\left(\boldsymbol{\Gamma}(s) \circ \mathrm{DFT}(\boldsymbol{f})\right), \tag{38}$$

where $\boldsymbol{\Gamma}(s)$ is a vector of size N, whose components are given by

$$\Gamma_i = \frac{1}{1 + s\xi_i^{2m}}. \tag{39}$$

The computational complexity of the smoother can thus be of $O(N\log(N))$ when FFT algorithms are used to perform the DFT and IDFT operations.

The smooth estimate $\tilde{\boldsymbol{f}}$ defined by (38) is controlled by the single parameter s. From the definition of the penalty term, it appears that, for a given value of s, the smoother is sensitive to the value of the period T. For instance, if the spatial period T is modified but the discretization remains the same, the penalty term is modified since $\Delta x = T/N$ is changed. This implies that the smoother is sensitive to some "length" through the period T. In order to make the smoothing parameter independent of the period T or the discretization N, it is necessary to consider some non-dimensional parameter $\bar{s}$. With the following definition of the smoothing parameter s

$$s = \bar{s}\, T^{2m} \tag{40}$$

a modification of the period T does not modify the smooth estimate, for a given value of $\bar{s}$.

4.2 Multidimensional smoothing of evenly spaced periodic data

Since a multidimensional DFT consists basically in a composition of one-dimensional DFT along each dimension, equation (38) can be easily extended to higher dimensions.

We are thus concerned with the smoothing of a periodic three-dimensional function f defined in the interval $[0,\ T] \times [0,\ T] \times [0,\ T]$ discretized with $N \times N \times N$ voxels. We consider a uniform

grid with spatial scales $\Delta x = \Delta y = \Delta z = T/N$ and we use the following notations: $x_j = j\Delta x$, $y_k = k\Delta_x$, $z_l = l\Delta x$, $f_{jkl} = f(x_j, y_k, z_l)$, with $0 \leq j \leq N-1$, $0 \leq k \leq N-1$ and $0 \leq l \leq N-1$. The discrete values of function f denoted f_{jkl} may thus be written as a $N \times N \times N$ hypermatrix denoted by $\boldsymbol{f}$. We are thus looking for the discrete values $\tilde{f}_{jkl}$ of the smooth estimate $\tilde{f}$, which consists in finding the hypermatrix $\tilde{\boldsymbol{f}}$.

The three-dimensional DFT can be formally written as

$$\hat{\boldsymbol{f}} = \mathrm{DFT3}(\boldsymbol{f}) = \mathbf{F}_3 \boldsymbol{f}, \tag{41}$$

where $\mathbf{F}_3$ is a symmetric $N \times N \times N \times N \times N \times N$ hypermatrix that can be constructed from $\mathbf{F}$. The associated Fourier frequency vectors to the grid vectors $\boldsymbol{x}$, $\boldsymbol{y}$ and $\boldsymbol{z}$ are respectively denoted by $\boldsymbol{\xi}$, $\boldsymbol{\upsilon}$ and $\boldsymbol{\zeta}$. The partial derivatives $\partial^m \boldsymbol{f}/\partial x^m$, $\partial^m \boldsymbol{f}/\partial y^m$ and $\partial \boldsymbol{f}/\partial z^m$ can be expressed in Fourier space and read

$$\frac{\partial^m \boldsymbol{f}}{\partial x^m} = \mathbf{D}_x \boldsymbol{f} = \imath^m \mathbf{F}_3^{-1} \left(\boldsymbol{\Lambda}_3^x\right)^m \circ \mathbf{F}_3 \boldsymbol{f}, \quad \frac{\partial^m \boldsymbol{f}}{\partial y^m} = \mathbf{D}_y \boldsymbol{f} = \imath^m \mathbf{F}_3^{-1} \left(\boldsymbol{\Lambda}_3^y\right)^m \circ \mathbf{F}_3 \boldsymbol{f}, \quad \frac{\partial^m \boldsymbol{f}}{\partial z^m} = \mathbf{D}_z \boldsymbol{f} = \imath^m \mathbf{F}_3^{-1} \left(\boldsymbol{\Lambda}_3^z\right)^m \circ \mathbf{F}_3 \boldsymbol{f}, \tag{42}$$

where $\boldsymbol{\Lambda}_3^x$, $\boldsymbol{\Lambda}_3^y$ and $\boldsymbol{\Lambda}_3^z$ are $N \times N \times N$ hypermatrices that are given by

$$\boldsymbol{\Lambda}^x_{3,jkl} = \xi_j \quad \forall (k,l), \qquad \boldsymbol{\Lambda}^y_{3,jkl} = \upsilon_k \quad \forall (j,l), \qquad \boldsymbol{\Lambda}^z_{3,jkl} = \zeta_l \quad \forall (j,k). \tag{43}$$

In the three-dimensional case, the penalty term reads

$$\left\|\mathbf{D}_x \tilde{\boldsymbol{f}}\right\|^2 + \left\|\mathbf{D}_y \tilde{\boldsymbol{f}}\right\|^2 + \left\|\mathbf{D}_z \tilde{\boldsymbol{f}}\right\|^2, \tag{44}$$

where the differentiation operators $\mathbf{D}_x$, $\mathbf{D}_y$ and $\mathbf{D}_z$ can be constructed using equation (42).

The minimization of the functional $\mathcal{F}$ leads to the expression of the smooth estimate $\tilde{\boldsymbol{f}}$

$$\tilde{\boldsymbol{f}} = \mathrm{IDFT3}\left(\boldsymbol{\Gamma}_3(s) \circ \mathrm{DFT3}(\boldsymbol{f})\right), \tag{45}$$

where $\boldsymbol{\Gamma}_3(s)$ is a $N \times N \times N$ hypermatrix whose components are given by

$$\Gamma_{3,jkl} = \frac{1}{1 + s(\xi_j^{2m} + \upsilon_k^{2m} + \zeta_l^{2m})}. \tag{46}$$

4.3 Comments

In the particular case of the first derivative in the penalty term ($m = 1$), corresponding to a spline of degree 1, it is worth noting that the smoother defined by equation (45) reduces to the (classical) smoother

$$\tilde{\boldsymbol{f}} - s\boldsymbol{\Delta}\tilde{\boldsymbol{f}} = \boldsymbol{f}, \tag{47}$$

where $\boldsymbol{\Delta}$ is the Laplacian operator. The smoother defined by equation (47) was initially introduced in the seminal paper of Mumford and Shah (1989) related to image segmentation problems and was notably used in the variational theory of brittle fracture (Francfort and Marigo, 1998). It should be noted that this smoother, if applied as a post-treatment of the solution fields, will add an extra regularity to the fields which will become C^1. This may lead to unphysical features of

the stress field in cases where it naturally presents singularities such as in the presence of cracks (Gasnier et al., 2018; Willot et al., 2020).

Hereafter we will restrict ourselves to the case $m = 1$ because higher-order splines may induce (i) too much regularity to the fields and (ii) several inflection points which are not desired because the smooth field can exceed the initial interval of values and leads to unphysical values (such as negative material properties in the case of pre-smoothing).

It should be also noted that, in the case of a post-smoother applied to each component of the stress field, the equilibrium equation will not be deteriorated. Indeed, the convergence criterion (15) will actually decrease as the numerator does not grow (the coefficients in equation (46) are always lower than 1) and the denominator remains the same.

5 Applications

In this Section, the periodic smoother developed in Section 4 is applied to problems of conductivity, elasticity and field dislocation mechanics. Both *pre-smoothing* (smoothing of the material discontinuities) and *post-smoothing* (smoothing of the solution field having oscillations) will be investigated separately.

5.1 Conductivity

5.1.1 Checkerboard-type microstructure

We begin with the classical problem of conductivity for checkerboard-type microstructures which is of interest since this problem has an analytical exact solution (Dykhne, 1971; Obnosov, 1999; Craster and Obnosov, 2001) (see also Bellis et al. (2020)). This problem was notably investigated in previous studies since it is highly challenging for the accurate description, without spurious oscillations[2], of the local fields (Willot et al., 2014; Dorn and Schneider, 2019).

For the numerical solution, we consider a 2D periodic square domain $[-1, 1] \times [-1, 1]$ discretized with 512×512 pixels. We consider that the isotropic conductivity field $c(x_1, x_2)$ field is heterogeneous and forms a checkerboard-type microstructure with discontinuous values $c_1 = 1$ and $c_2 = 100$ as shown in Figure 4a. The values $\overline{E}_1 = 1$ and $\overline{E}_2 = 0$ are considered for the prescribed macroscopic electric field $\overline{\mathbf{E}}$. Convergence of the iterative procedure is reached when the error defined by equation (15) is smaller than the prescribed value 10^{-5}, which corresponds in that case to about 350 iterations.

Smoothing of material properties (pre-smoothing) First we investigate the effect of the smoother on the *initial* conductivity field $c(x_1, x_2)$. The heterogeneous field $c(x_1, x_2)$ is smoothed using two values of the parameter $\bar{s} = 5 \times 10^{-6}$ and $\bar{s} = 5 \times 10^{-5}$. The effect of parameter $\bar{s}$ on the microstructure is illustrated in Figure 4. The difference between smoothed and initial microstructure is very small; only the transition between the two phases seems affected by the

[2] It is worth noting that in this conductivity problem, the discrete Green operator proposed by Willot et al. (2014) does not produce oscillations.

smoother, notably at the corners.

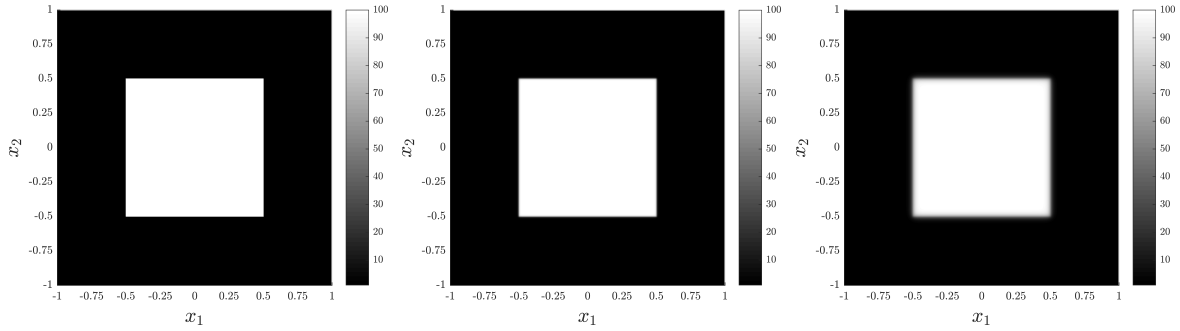

(a) (b) (c)

Fig. 4. Distribution of the heterogeneous field $c(x_1, x_2)$. (a) Case $s = 0$ (no smooth), (b) Case $\bar{s} = 5\times10^{-6}$, (c) Case $\bar{s} = 5 \times 10^{-5}$.

An enlarged view, at the vicinity of the interface between the two phases, is plotted in Figure 5, on the line $x_2 = 0$, which permits to show the effect of the smoother. The smoother creates a finite and smoothed transition zone between the two phases. The thickness of this transition zone increases when the smoothing parameter s increases.

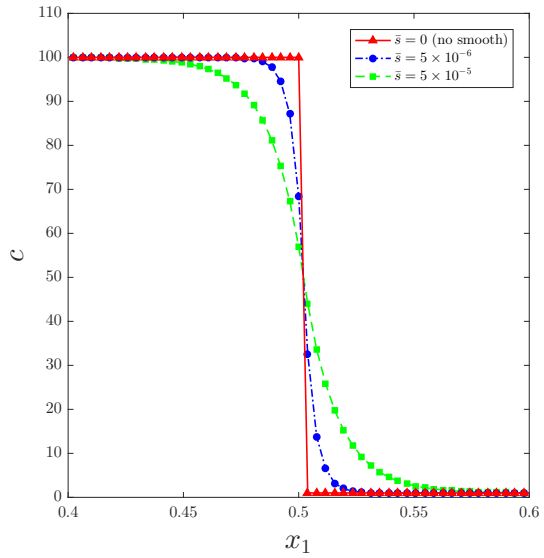

Fig. 5. Effect of smoothing on the microstructure on the line $x_2 = 0$.

The checkerboard problem is thus solved for these three microstructures and the numerical results together with the analytical solution are represented, on the whole domain and near the top corner, in Figure 6. The distribution of the normalized electric current $J_1/\left\|\bar{\mathbf{J}}\right\|$ presents important spurious oscillations in the case $s = 0$ (initial microstructure). The use of the smoother permits to erase the oscillations but also results in a spreading of the solution which become more diffuse than the exact one. Overall the numerical distributions of the normalized current are very similar irrespective of the smoothing, in terms of morphology and intensity, and are close to the analytical solution.

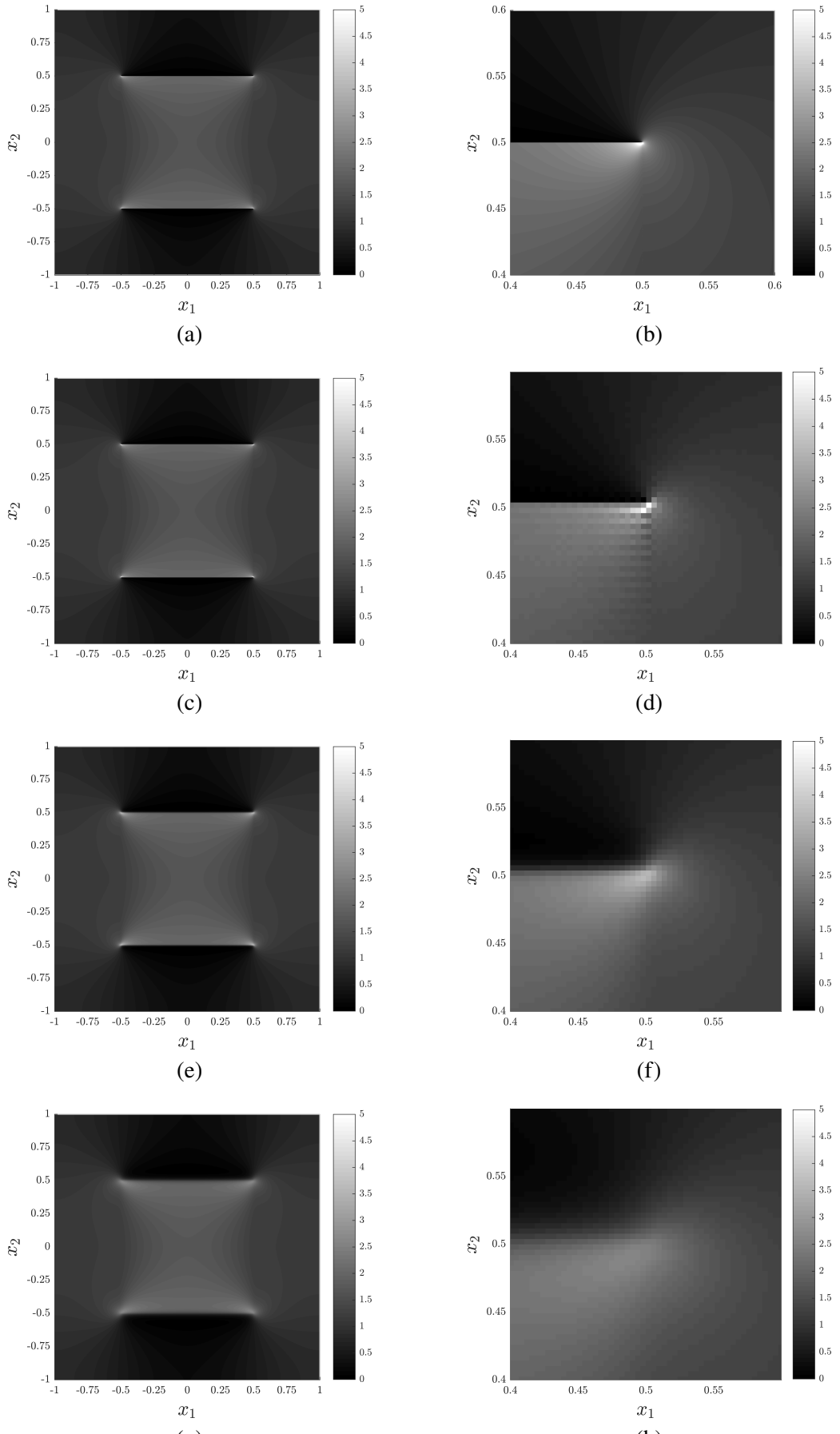

Fig. 6. Distribution of the normalized electric current $J_1/\left\|\bar{\mathbf{J}}\right\|$. (a-b) Analytical solution, (c-d) Case $s = 0$ (no smooth), (e-f) Case $\bar{s} = 5 \times 10^{-6}$, (g-h) Case $\bar{s} = 5 \times 10^{-5}$.

Smoothing of the solution field (post-smoothing) We investigate now the effect of the smoother as a post-treatment of the solution J_1 having oscillations, calculated for the checkerboard without initial smooth (represented in Figure 4a). Thus the smoother is directly applied to the field J_1 with oscillations that was represented in Figure 6c. The values $\bar{s} = 5 \times 10^{-6}$ and $\bar{s} = 5 \times 10^{-5}$ are considered and the results are represented in Figure 7. In that case, where smoothing is performed as a post-treatment, the oscillations are erased and the numerical distribution of normalized electric current $J_1 / \left\| \bar{\mathbf{J}} \right\|$ is very close to the exact solution field. Again, an increase of the smoothing parameter leads to a spreading of the solution.

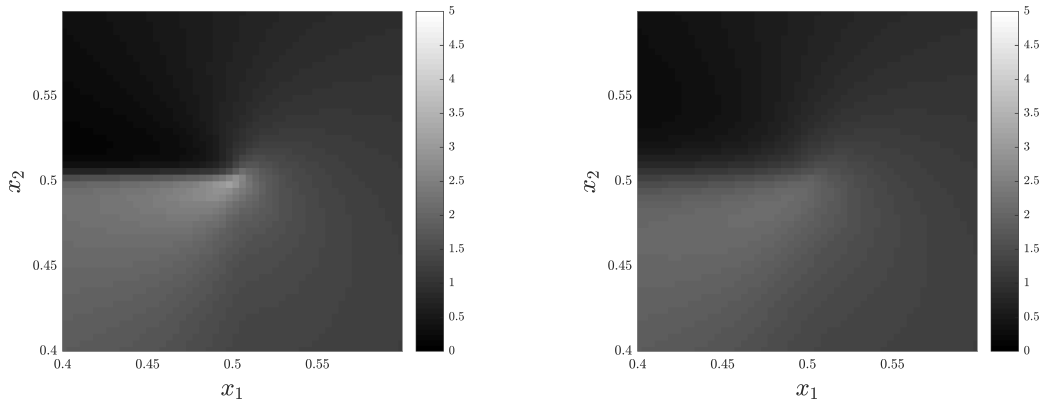

Fig. 7. Effect of the smoother as a post-treatment on the distribution of the normalized electric current $J_1 / \left\| \bar{\mathbf{J}} \right\|$. (a) Case $\bar{s} = 5 \times 10^{-6}$, (b) Case $\bar{s} = 5 \times 10^{-5}$.

Comparison with the analytical solution The normalized electric current $J_1 / \left\| \bar{\mathbf{J}} \right\|$ is now quantitatively compared to the exact solution in Figure 8, on the line $x_2 = 0.5$ close to the top corner. The non-smoothed electrical field ($\bar{s} = 0$) is affected by strong oscillations that are completely removed by the smoother in both cases (pre-treatment or post-treatment). It is interesting to note that pre-smoothing acts as a regularization of the material discontinuity which results in a diffuse spreading of the solution while post-smoothing acts directly on the oscillations so it results in a spreading effect more important but less diffuse.

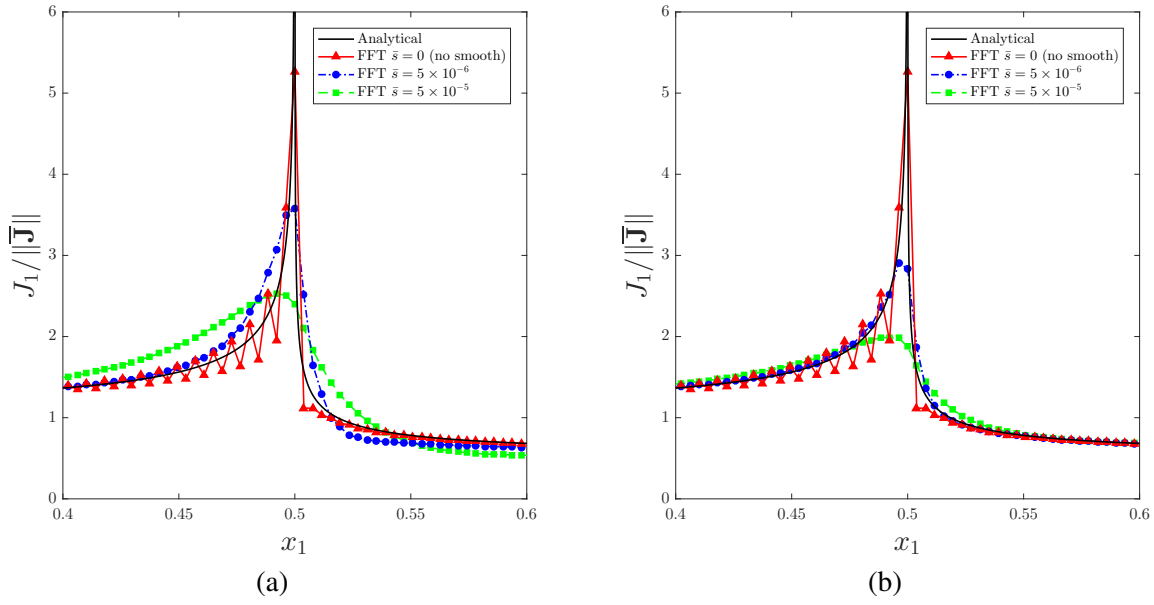

Fig. 8. Effect of smoothing on the normalized electric current $J_1 / \left\| \bar{\mathbf{J}} \right\|$ on the line $x_2 = 0.5$. (a) Smoothing of the material field $c(x_1, x_2)$ and (b) Smoothing of the computed field $J_1(x_1, x_2)$ with oscillations as a post-treatment.

5.1.2 *Rotated checkerboard-type microstructure*

We now consider a rotated checkerboard-type microstructure which is an interesting problem since in that case the discontinuity is arbitrary as it is not aligned anymore with the spatial grid. For the numerical solution, we consider a 2D periodic square domain $[-1,1]\times[-1,1]$ discretized with 512×512 pixels. The conductivity field $c(x_1, x_2)$ field forms a rotated checkerboard-type microstructure as shown in Figure 9a. The values $\overline{E}_1 = 1$ and $\overline{E}_2 = 0$ are considered for the prescribed macroscopic electric field $\overline{\mathbf{E}}$. Convergence of the iterative procedure is reached when the error defined by equation (15) is smaller than the prescribed value 10^{-5}.

First, we investigate the effect of the smoother on the *initial* conductivity field $c(x_1, x_2)$. The heterogeneous field $c(x_1, x_2)$ is smoothed out by using two values of the parameter $\bar{s} = 5 \times 10^{-6}$ and $\bar{s} = 5 \times 10^{-5}$ and the effect of parameter $\bar{s}$ on the microstructure is illustrated in Figure 9. The numerical results are provided in Figure 10.

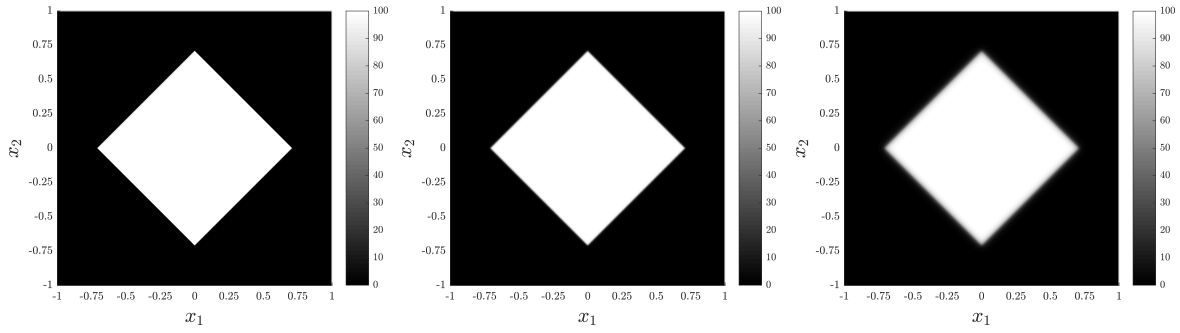

(a) (b) (c)

Fig. 9. Distribution of the heterogeneous field $c(x_1, x_2)$ in the case of the rotated checkerboard. (a) Case $s = 0$ (no smooth), (b) Case $\bar{s} = 5 \times 10^{-6}$, (c) Case $\bar{s} = 5 \times 10^{-5}$.

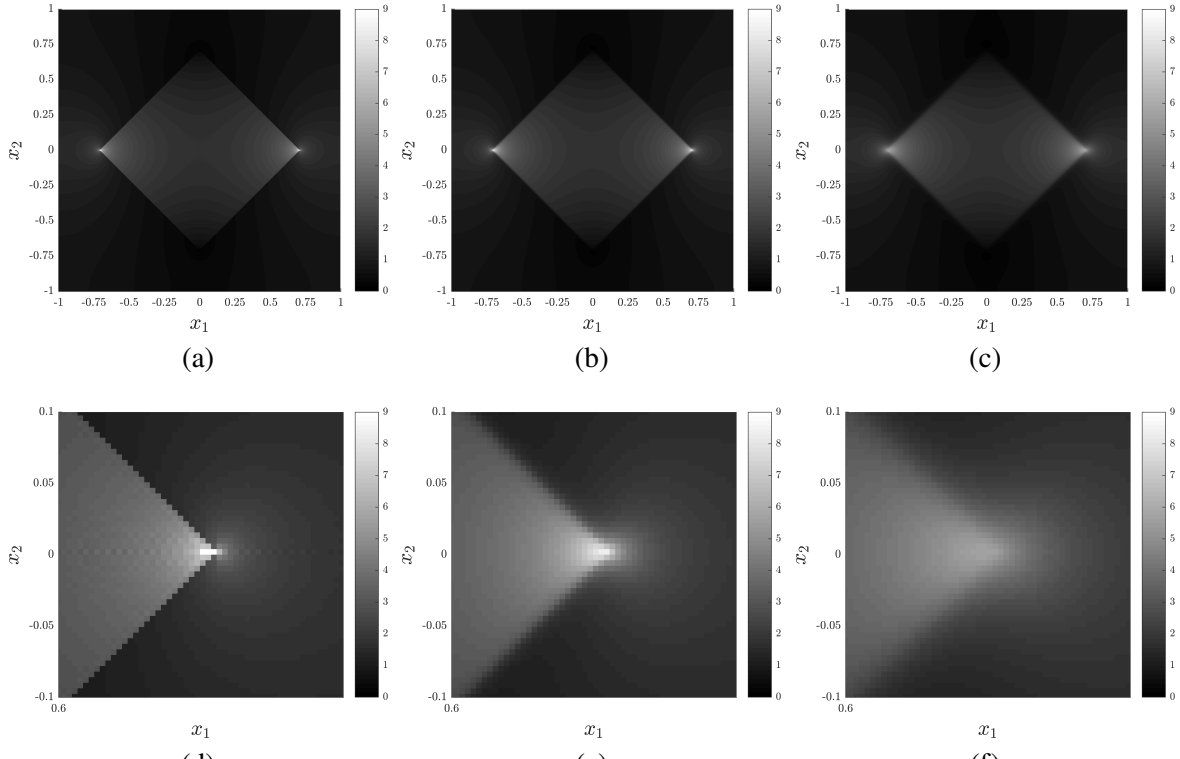

(a) (b) (c)

(d) (e) (f)

Fig. 10. Distribution of the normalized electric current $J_1 / \left\| \overline{\mathbf{J}} \right\|$ in the case of the rotated checkerboard. (a) Case $s = 0$ (no smooth), (b) Case $\bar{s} = 5 \times 10^{-6}$, (c) Case $\bar{s} = 5 \times 10^{-5}$, (d) Case $s = 0$ (enlarged view), (e) Case $\bar{s} = 5 \times 10^{-6}$ (enlarged view), (f) Case $\bar{s} = 5 \times 10^{-5}$ (enlarged view).

The oscillations observed in the discontinuous case ($\bar{s} = 0$) are erased by the use of the smoother. As expected, the smoother permits to capture the discontinuity that is not aligned with the grid, allowing to treat arbitrary microstructures. Then, we consider the effect of the smoother as a *post-treatment* on the solution field J_1 calculated for the rotated checkerboard without initial smooth. The results are provided in Figure 11. The distribution of the normalized electric current $J_1/\left\|\bar{\mathbf{J}}\right\|$ after smoothing reveals that spurious oscillations are no longer present.

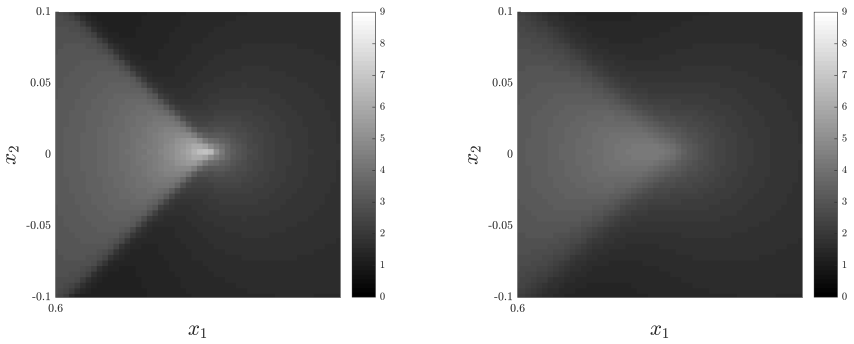

(a) (b)

Fig. 11. Effect of the smoother as a post-treatment on the distribution of the normalized electric current $J_1/\left\|\bar{\mathbf{J}}\right\|$ in the case of the rotated checkerboard. (a) Case $\bar{s} = 5 \times 10^{-6}$, (b) Case $\bar{s} = 5 \times 10^{-5}$.

5.2 Elasticity

We consider a plane strain problem of elasticity. In that case, the displacement field $\boldsymbol{u}^*$ is of the form

$$\boldsymbol{u}^* = u_1^*(x_1, x_2)\boldsymbol{e}_1 + u_2^*(x_1, x_2)\boldsymbol{e}_2, \tag{48}$$

and the not-null components of the strain and stress tensors are respectively $(\epsilon_{11}^*,\ \epsilon_{12}^*,\ \epsilon_{22}^*)$ and $(\sigma_{11},\ \sigma_{12},\ \sigma_{22},\ \sigma_{33})$. A 2D periodic square domain $[-1, 1] \times [-1, 1]$ containing a single circular inclusion (with volume fraction of about 19.63%) is discretized with 512×512 pixels. The microstructure is made of two phases whose properties are given by $E_m = 1$ and $\nu_m = 0.25$ in the matrix and $E_p = 100$ and $\nu_p = 0.25$ in the circular particle; the distribution of the discontinuous Young's modulus $E(x_1, x_2)$ is shown in Figure 12.

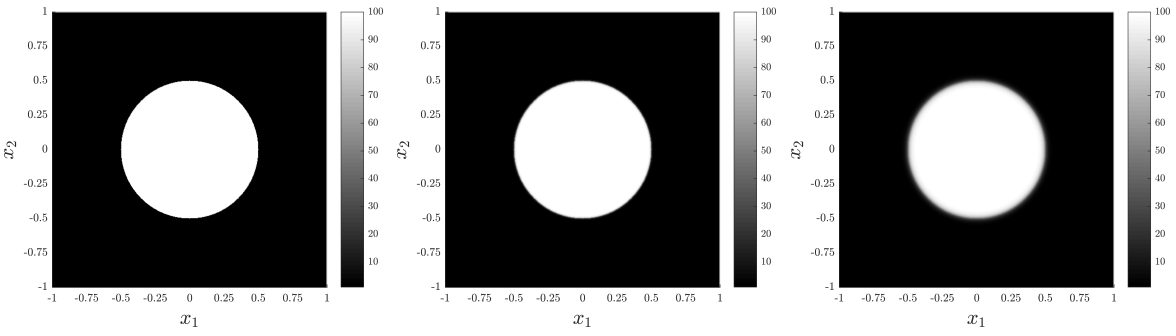

(a) (b) (c)

Fig. 12. Distribution of the Young's modulus field $E(x_1, x_2)$ in the elasticity problem. (a) Case $s = 0$ (no smooth), (b) Case $\bar{s} = 5 \times 10^{-6}$, (c) Case $\bar{s} = 5 \times 10^{-5}$.

First we investigate the effect of the smoother on the *initial* Young's modulus field $E(x_1, x_2)$: the heterogeneous field $E(x_1, x_2)$ is smoothed using two values of the parameter $\bar{s} = 5 \times 10^{-6}$ and $\bar{s} = 5 \times 10^{-5}$. The effect of parameter $\bar{s}$ on the microstructure is illustrated in Figure 12. For the simulations, the non-zero component of the prescribed macroscopic strain tensor is $\overline{\epsilon}_{12} = 1$.

As in the conductivity case, convergence of the iterative procedure is reached when the error defined by equation (15) is smaller than the prescribed value 10^{-5}, which corresponds in that case to about 450 iterations.

The numerical distributions of the normalized local shear stress $\sigma_{12}/\overline{\sigma}_{12}$ are represented, on the whole domain and on an enlarged view in the domain $[-0.6, -0.3] \times [0, 0.3]$, in Figure 13. In the case $\bar{s} = 0$ (initial discontinuous microstructure), strong oscillations are observed in the entire domain, especially near the interface between the matrix and the particle. The use of the smoother permits to erase these oscillations and to provide maps of shear stress which are very close, in terms of morphology and intensity, to that predicted in the initial case. It is however important to note that an increase of the smoothing parameter necessarily leads to a spreading of the solution which may become different from that of the initial microstructure since the microstructure is modified by the smoother.

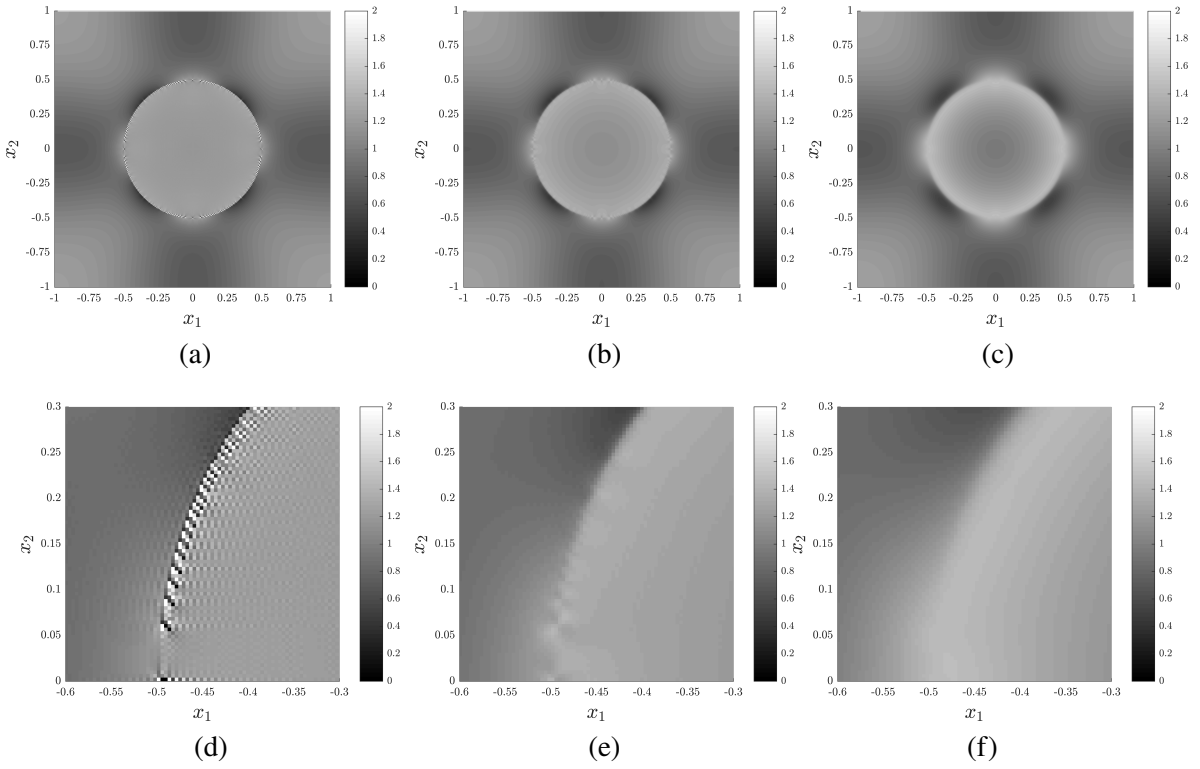

Fig. 13. Effect of properties smoothing on the distribution of the normalized shear stress $\sigma_{12}/\overline{\sigma}_{12}$. (a) Case $s = 0$ (no smooth), (b) Case $\bar{s} = 5 \times 10^{-6}$, (c) Case $\bar{s} = 5 \times 10^{-5}$, (d) Case $s = 0$ (enlarged view), (e) Case $\bar{s} = 5 \times 10^{-6}$ (enlarged view), (f) Case $\bar{s} = 5 \times 10^{-5}$ (enlarged view).

Then we consider the effect of the smoother on the shear stress solution field σ_{12} calculated without initial smoothing (see Figure 13a). The smoother is thus applied as a post-treatment to the field σ_{12} with oscillations. We consider as before the values $\bar{s} = 5 \times 10^{-6}$ and $\bar{s} = 5 \times 10^{-5}$ for the smoothing parameter and the results are provided in Figure 14.

It is interesting to note that, in the case $\bar{s} = 5 \times 10^{-6}$, small oscillations remains in the normalized shear stress field $\sigma_{12}/\overline{\sigma}_{12}$. Thus in that case, the oscillations are not entirely removed if the smoother is used as a post-treatment while they were erased by the smoothing of material properties. The case $\bar{s} = 5 \times 10^{-5}$ shows that an increase of the smoothing parameter permits however to suppress the oscillations even when post-treatment smoothing is considered.

The evolution of the σ_{12} stress component along the line $x_2 = 0$ is represented in Figure 15. In both cases (*pre-* or *post-treatment* smoothing), the oscillations are greatly decreased.

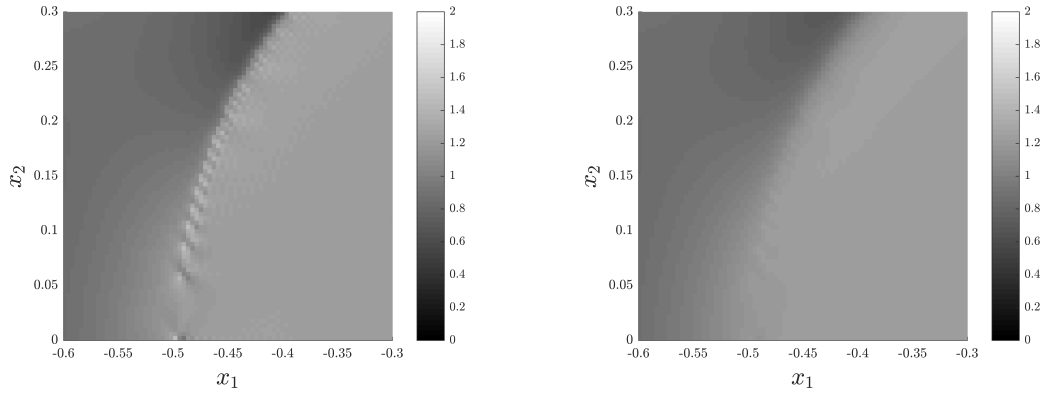

Fig. 14. Effect of the smoother as a post-treatment on the distribution of the normalized shear stress $\sigma_{12}/\overline{\sigma}_{12}$. (a) Case $\bar{s} = 5 \times 10^{-6}$, (b) Case $\bar{s} = 5 \times 10^{-5}$.

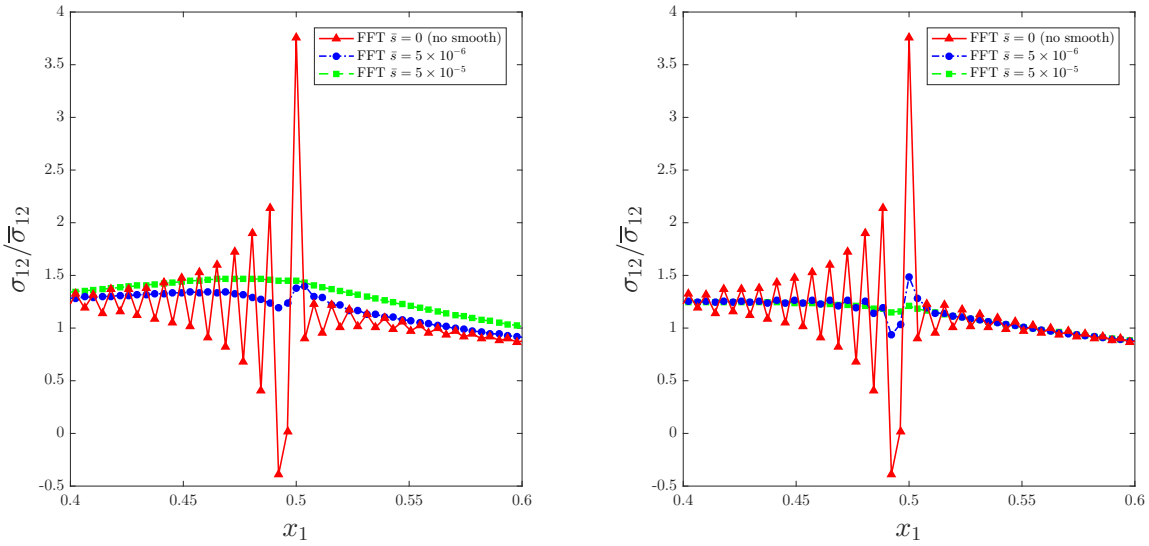

Fig. 15. Effect of smoothing on the normalized shear stress $\sigma_{12}/\overline{\sigma}_{12}$ on the line $x_2 = 0$. (a) Smoothing of the material field $E(x_1, x_2)$ and (b) Smoothing of the computed field $\sigma_{12}(x_1, x_2)$ with oscillations as a post-treatment.

5.3 Field dislocation mechanics

As a last example, we address a problem encountered in field dislocation mechanics when the Nye dislocation tensor field $\boldsymbol{\alpha}(\boldsymbol{x})$ presents discontinuities. Oscillations in the stress solution field have been reported in the case of a pixel-wise dislocation density to represent a single dislocation (Brenner et al., 2014).

We consider the anti-plane strain problem for a single screw dislocation with isotropic elasticity. The displacement field is of the form

$$\boldsymbol{u}^* = u_3^*(x_1, x_2)\boldsymbol{e}_3 \tag{49}$$

and the non-zero components of the strain and stress tensors are respectively $(\epsilon_{13}^*,\ \epsilon_{23}^*)$ and $(\sigma_{13},\ \sigma_{23})$. In the case of an infinite medium, the classical analytical solution for the stress field reads

$$\boldsymbol{\sigma}_{13}(x_1, x_2) = -\frac{\mu b}{2\pi}\frac{x_2}{x_1^2 + x_2^2}, \quad \boldsymbol{\sigma}_{23}(x_1, x_2) = \frac{\mu b}{2\pi}\frac{x_1}{x_1^2 + x_2^2}. \tag{50}$$

Following Brenner et al. (2014), we consider a 2D unit-cell domain of $318b \times 318b$, with b the norm of the Burgers vector, discretized on a regular grid of 1024×1024 pixels. For the numerical applications, we have chosen the value $b = 0.286\,\text{nm}$ which corresponds to aluminium (CFC crystalline structure) and we have prescribed a dislocation density $\alpha_{33} = 4.0 \times 10^9\,\text{m}^{-1}$ at a single pixel.

The evolution of the σ_{23} stress component along the line $x_2 = 0$ is represented in Figure 16 for different values of the non-dimensional parameter $\bar{s}$ and compared to the analytical solution which exhibits a $1/x_1$ dependence. As expected, the oscillations are erased and a reasonable smooth estimate is obtained for $\bar{s} = 5 \times 10^{-6}$. By contrast with the conductivity and elasticity problems, the material discontinuity is only due to the prescribed eigenstress field since we deal with homogeneous elasticity (i.e single crystal). In this particular case, it must be noted that there is no difference between the smoothers used as *pre-* or *post-treatment*.

The 2D distribution of the σ_{23} stress component is reported in Figure 17. This highlights the spreading effect of the smoother. It can be remarked that the oscillations for $\bar{s} = 0$ only occur along the line $x_2 = 0$.

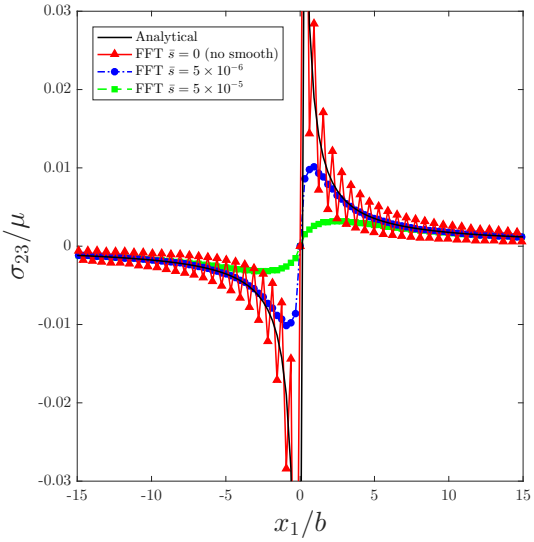

Fig. 16. Effect of smoothing on the normalized stress σ_{23}/μ on the line $x_2 = 0$.

6 Conclusion

The aim of this paper was to develop a periodic smoother based on splines in order to decrease spurious oscillations observed on local fields computed by FFT-based solvers in problems governed by elliptic equations. First, the conditions of emergence of spurious oscillations have been investigated; it has been shown that these oscillations may initiate in FFT-based solvers when the polarization field has some discontinuities and when pseudo-spectral differentiation is used. A three-dimensional spline smoother was then developed, based on the minimization of a functional balancing the fidelity of the data and the smoothness of the estimate; the degree of smoothness is controlled by a scalar which sets the size of the zone affected by smoothing. Several discontinuous microstructures have finally been investigated in problems of conductivity, elasticity and field dislocation mechanics. The smoother, applied to the initial microstructure as a pre-treatment, creates a finite and smooth transition zone between phases whose size is controlled by the smoothing parameter, permitting to erase spurious oscillations observed on

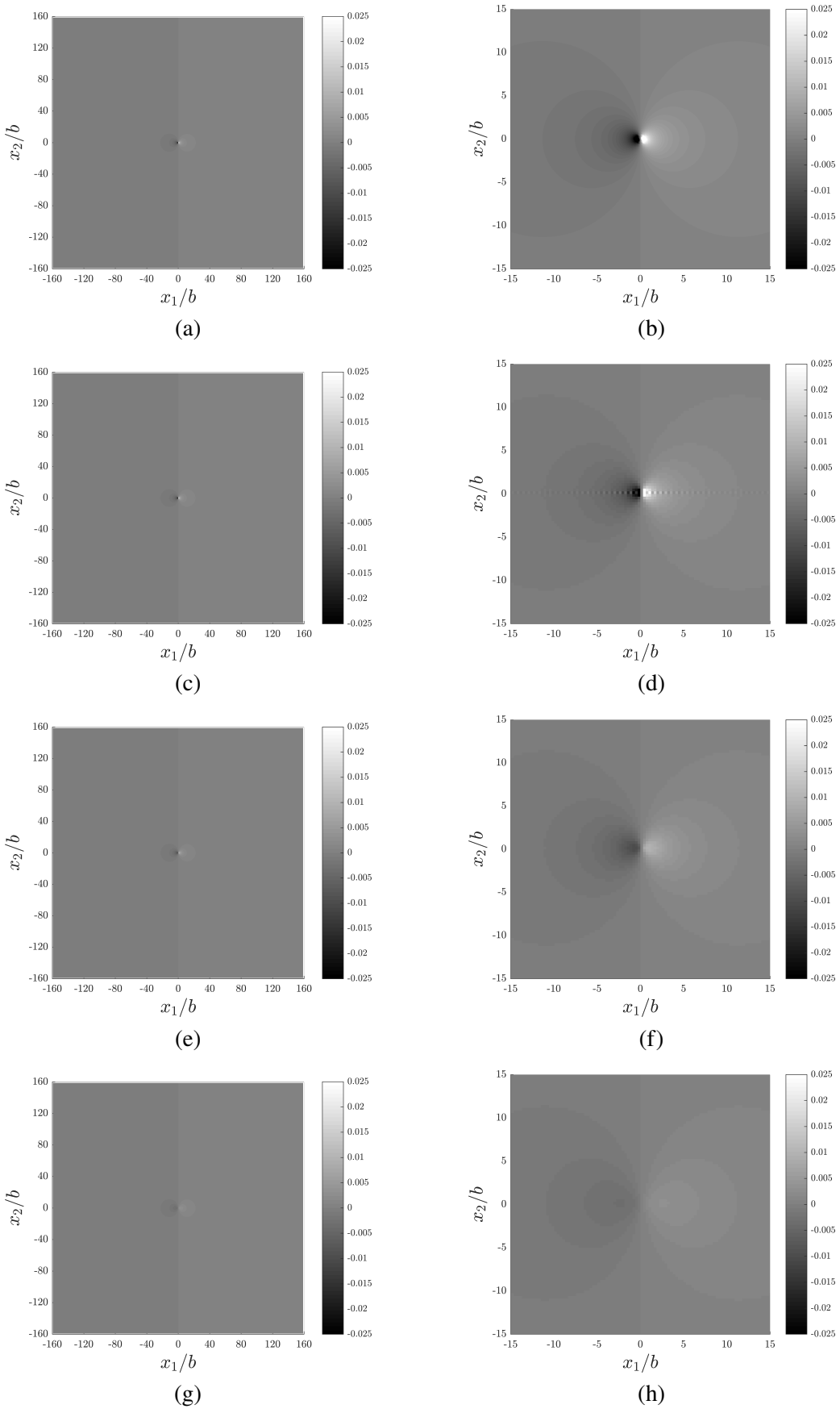

Fig. 17. Distribution of the normalized stress σ_{23}/μ. (a-b) Analytical solution, (c-d) Case $s = 0$ (no smooth), (e-f) Case $\bar{s} = 5 \times 10^{-6}$, (g-h) Case $\bar{s} = 5 \times 10^{-5}$.

local fields at the expense of some spreading of the solution. The smoother, applied to the local solution field having artifacts, leads to a significant decrease (if not a complete suppression) of

oscillations.

The *pre-smoother* thus appears particularly suitable in the case of microstructures with *interphases*. Indeed, the pre-treatment smoothing of material properties creates a finite and smooth transition zone between phases which corresponds to some interphase whose size can be controlled by the smoothing parameter. The *post-smoother*, on the other hand, appears more suitable in the case of *interfaces* between phases. In that case, the calculations can be performed using the microstructure having interfaces, and the smoother is applied as post-treatment on the computed local fields; this allows to erase oscillations which is of interest when precise local fields are looked for near an interface.

The advantages of the method proposed in this work are three-fold:

(1) It can be used as a pre-treatment on the discontinuous material field or as a post-treatment on the solution field having oscillations, without any modification of the FFT-based solver.
(2) It relies on the computation of Fourier transforms which makes its implementation very efficient in terms of computational cost.
(3) It does not require the prior detection of the interfaces (and the definition of the associated normal) as it operates globally on the discontinuous field.

The main disadvantage of the method is that the (smooth) local fields obtained with it depend on the value of the smoothing parameter. This implies that a proper estimation of this parameter is necessary in order to get a good compromise between the suppression of oscillations and the spreading of the solution:

- In the case of the *post-smoother*, the aim of the smoothing is to erase oscillations. In essence, this problem is very similar to the problem of removing noise in a signal, so classical techniques of generalized cross-validation (GCV) can be used in that case to estimate the optimal value of the smoothing parameter (Craven and Wahba, 1979; Garcia, 2010).
- In the case of the *pre-smoother*, generalized cross-validation methods cannot be used because there is no noise to smooth out and an extra smoothing is looked for. A possible criterion for selecting the smoothing parameter could be related to the thickness of the interphase between phases, whose maximum admissible value would be estimated based on physical considerations.

It is worth noting that the periodic smoother can be naturally applied in other situations, including notably (i) the smoothing of uniformly sampled periodic datasets to reduce experimental noise and/or deal with the occurrence of missing values and (ii) the generation of periodic microstructures from non-periodic images (obtained by SEM for instance) through the smoothing of the discontinuous boundaries.

Acknowledgement

Fruitful discussions with H. Moulinec and P. Suquet are gratefully acknowledged.

References

Acharya, A., 2001. A model of crystal plasticity based on the theory of continuously distributed dislocations. Journal of the Mechanics and Physics of Solids 49, 761–784.

Bellis, C., Moulinec, H., Suquet, P., 2020. Eigendecomposition-based convergence analysis of the Neumann series for laminated composites and discretization error estimation. International Journal for Numerical Methods in Engineering 121, 201–232.

Berbenni, S., Taupin, V., Djaka, K.S., Fressengeas, C., 2014. A numerical spectral approach for solving elasto-static field dislocation and g-disclination mechanics. International Journal of Solids and Structures 51, 4157–4175.

Berrut, J.P., Reifenberg, M., 1997. Numerical solution of periodic Fredholm integral equations of the second kind by means of attenuation factors. The Journal of Integral Equations and Applications 9, 1–20.

Bertin, N., Upadhyay, M.V., Pradalier, C., Capolungo, L., 2015. A FFT-based formulation for efficient mechanical fields computation in isotropic and anisotropic periodic discrete dislocation dynamics. Modelling and Simulation in Materials Science and Engineering 23, 065009.

Brenner, R., 2009. Numerical computation of the response of piezoelectric composites using Fourier transform. Phys. Rev. B 79, 184106.

Brenner, R., Beaudoin, A.J., Suquet, P., Acharya, A., 2014. Numerical implementation of static Field Dislocation Mechanics theory for periodic media. Philosophical Magazine 94, 1764–1787.

Brisard, S., Dormieux, L., 2012. Combining Galerkin approximation techniques with the principle of Hashin and Shtrikman to derive a new FFT-based numerical method for the homogenization of composites. Computer Methods in Applied Mechanics and Engineering 217-220, 197–212.

Brown, C.M., Dreyer, W., Müller, W.H., 2002. Discrete Fourier transforms and their application to stress—strain problems in composite mechanics: a convergence study. Proceedings of the Royal Society of London. Series A: Mathematical, Physical and Engineering Sciences 458, 1967–1987.

Buckley, M.J., 1994. Fast Computation of a Discretized thin-Plate Smoothing Spline for Image Data. Biometrika 81, 247–258.

Cai, W., Gottlieb, D., Shu, C.W., 1992. On One-Sided Filters for Spectral Fourier Approximations of Discontinuous Functions. SIAM Journal on Numerical Analysis 29, 905–916.

Charière, R., Marano, A., Gélébart, L., 2020. Use of composite voxels in FFT based elastic simulations of hollow glass microspheres/polypropylene composites. Int. J. Solids Struct. 182-183, 1–14.

Craster, R.V., Obnosov, Y.V., 2001. Four-Phase Checkerboard Composites. SIAM Journal on Applied Mathematics 61, 1839–1856.

Craven, P., Wahba, G., 1979. Smoothing noisy data with spline functions. Numerische Mathematik 31, 377–403.

Djaka, K.S., Berbenni, S., Taupin, V., Lebensohn, R.A., 2020. A FFT-based numerical implementation of mesoscale field dislocation mechanics: Application to two-phase laminates. International Journal of Solids and Structures 184, 136-152.

Dorn, C.,Schneider, M., 2019. Lippmann-Schwinger solvers for the explicit jump discretization for thermal computational homogenization problems. International Journal for Numerical Methods in Engineering 118, 631-653.

Dykhne, A. M. 1971. Conductivity of a two-dimensional two-phase system. Soviet Physics JETP 32, 63–65.

Eilers, P.H.C., 2003. A Perfect Smoother. Analytical Chemistry 75, 3631–3636.

Eloh, K.S., Jacques, A., Berbenni, S., 2018. Development of a new consistent discrete Green operator for FFT-based methods to solve heterogeneous problems with eigenstrains. International Journal of Plasticity 116, 1–23.

Eyre, D.J., Milton, G.W., 1999. A fast numerical scheme for computing the response of composites using grid refinement*. The European Physical Journal - Applied Physics 6, 41–47.

Fornberg, B., 1987. The pseudospectral method: Comparisons with finite differences for the elastic wave equation. GEOPHYSICS 52, 483–501.

Francfort, G.A., Marigo, J.J., 1998. Revisiting brittle fracture as an energy minimization problem. Journal of the Mechanics and Physics of Solids 46, 1319–1342.

Garcia, D., 2010. Robust smoothing of gridded data in one and higher dimensions with missing values. Computational Statistics & Data Analysis 54, 1167–1178.

Gasnier, J.B., Willot, F., Trumel, H., Jeulin, D., Besson, J., 2018. Thermoelastic properties of microcracked polycrystals. Part I: Adequacy of Fourier-based methods for cracked elastic bodies. International Journal of Solids and Structures 155, 248–256.

Gélébart, L., Ouaki, F., 2015. Filtering material properties to improve FFT-based methods for numerical homogenization. Journal of Computational Physics 294, 90–95.

Hastie, T., Loader, C., 1993. Local Regression: Automatic Kernel Carpentry. Statistical Science 8, 120–129.

Kabel, M., Merkert, D., Schneider, M., 2015. Use of composite voxels in FFT-based homogenization. Computer Methods in Applied Mechanics and Engineering 294, 168–188.

Lebensohn, R., 2001. N-site modeling of a 3d viscoplastic polycrystal using Fast Fourier Transform. Acta Materialia 49, 2723–2737.

Michel, J.C., Moulinec, H., Suquet, P., 2000. A computational method based on augmented Lagrangians and fast Fourier transforms for composites with high contrast. Computer Modelling in Engineering & Sciences 1, 79–88.

Monchiet, V., Bonnet, G., 2012. A polarization-based FFT iterative scheme for computing the effective properties of elastic composites with arbitrary contrast. International Journal for Numerical Methods in Engineering 89, 1419–1436.

Morin, L., Brenner, R., Suquet, P., 2019. Numerical simulation of model problems in plasticity based on field dislocation mechanics. Modelling and Simulation in Materials Science and Engineering 27, 085012.

Moulinec, H., Suquet, P., 1998. A numerical method for computing the overall response of nonlinear composites with complex microstructure. Computer Methods in Applied Mechanics and Engineering 157, 69–94.

Moulinec, H., Silva, F., 2014. Comparison of three accelerated FFT-based schemes for computing the mechanical response of composite materials. International Journal for Numerical Methods in Engineering 97, 960–985.

Müller, W.H., 1996. Mathematical vs. Experimental Stress Analysis of Inhomogeneities in Solids. Le Journal de Physique IV 06, C1–139–C1–148.

Mumford, D.B., Shah, J., 1989. Optimal approximations by piecewise smooth functions and associated variational problems. Communications on pure and applied mathematics.

Obnosov, Y.V., 1999. Periodic Heterogeneous Structures: New Explicit Solutions and Effective Characteristics of Refraction of an Imposed Field. SIAM Journal on Applied Mathematics 59, 1267–1287.

Savitzky, A., Golay, M.J., 1964. Smoothing and differentiation of data by simplified least squares procedures. Analytical chemistry 36, 1627–1639.

Schoenberg, I.J., 1964. Spline Functions and the Problem of Graduation. Proceedings of the National Academy of Sciences 52, 947–950.

Schneider, M., 2020. Lippmann-Schwinger solvers for the computational homogenization of materials with pores. International Journal for Numerical Methods in Engineering (In Press).

Suquet, P., Moulinec, H., Castelnau, O., Montagnat, M., Lahellec, N., Grennerat, F., Duval, P., Brenner, R., 2012. Multi-scale modeling of the mechanical behavior of polycrystalline ice under transient creep. Procedia IUTAM 3, 76–90.

Vandeven, H., 1991. Family of spectral filters for discontinuous problems. Journal of Scientific Computing 6, 159–192.

van Vliet, L.J., Young, I.T., Beckers, G.L., 1989. A nonlinear laplace operator as edge detector in noisy images. Computer Vision, Graphics, and Image Processing 45, 167–195.

Vidyasagar, A., Tan, W. L., Kochmann, D. M., 2017. Predicting the effective response of bulk polycrystalline ferroelectric ceramics via improved spectral phase field methods. J. Mech. Phys. Solids 106, 133–151.

Wang, B., Fang, G., Liu, S., Liang, J., Lv, D., 2020. Smoothing interface stress oscillation of composite materials in FFT method by laminate theory. Mechanics of Advanced Materials and Structures (In Press).

Whittaker, E.T., 1922. On a New Method of Graduation. Proceedings of the Edinburgh Mathematical Society 41, 63–75.

Willot, F., 2015. Fourier-based schemes for computing the mechanical response of composites with accurate local fields. Comptes Rendus Mécanique 343, 232–245.

Willot, F., Abdallah, B., Pellegrini, Y.P., 2014. Fourier-based schemes with modified Green operator for computing the electrical response of heterogeneous media with accurate local fields. International Journal for Numerical Methods in Engineering 98, 518–533.

Willot, F., Brenner, R., Trumel, H., 2020. Elastostatic field distributions in polycrystals and cracked media. Philosophical Magazine 100, 661–687.